

Direct numerical simulation of a turbulent boundary layer separating over a curved wall using FastRK3

A. B. Aithal and A. Ferrante

Corresponding author: ferrante@aa.washington.edu

William E. Boeing Department of Aeronautics & Astronautics,
University of Washington, Seattle, USA

Abstract: Flow separation, resulting from an adverse pressure gradient (APG), is encountered in many engineering applications, however, the physical mechanisms of separated turbulent boundary layers over curved walls are not yet well understood. The wall models employed in Reynolds-averaged Navier-Stokes (RANS) and large-eddy simulations (LES) of such flows are not predictive tools and need to be improved. In order to provide the necessary statistics for the validation of such models and explain the physical mechanisms of such flows, we have performed direct numerical simulations (DNS) of a spatially developing turbulent boundary layer over a curved wall with APG using our new projection-method called FastRK3. FastRK3 is a three-stage, third-order Runge-Kutta projection-method for the incompressible Navier-Stokes equations, which requires solving the Poisson equation for pressure only once per time step. In the current work, we employ FastRK3 to perform DNS of a spatially developing turbulent boundary layer separating over a curved ramp and study the dynamics of its turbulence kinetic energy and Reynolds stresses.

Keywords: Pressure-correction method, explicit Runge-Kutta, fast Poisson solver, flow separation, turbulent flows, direct numerical simulation.

1 Introduction

Flow separation is referred to the flow reversal that occurs when the wall shear stress vanishes due to the adverse pressure gradient (APG) over curved bodies, and is accompanied by thickening of the boundary layer, a vortex filled wake and increased values of wall-normal component of velocity [1]. The prediction and control of separated flows are complicated due to their unsteadiness, three-dimensionality, and vortex-filled wakes. Reynolds averaged Navier-Stokes (RANS) wall-models fail when flow separation occurs [2, 3]. There is a need to develop a deeper understanding of the physical mechanisms of separated turbulent flows to improve the RANS wall-models, which are often also employed in wall-modeled large-eddy simulations (WMLES) and hybrid RANS/LES methods. Mollicone et al. [4] conducted direct numerical simulation (DNS) to study the effects of geometry and Reynolds number on the separated flow over a bulge in a turbulent channel flow. Recently, Balin and Jansen [5] conducted DNS of a turbulent boundary layer separating over a Gaussian-shaped bump and studied the relaminarization of the flow over the bump. However, a detailed study of the budgets of the Reynolds stress tensor, and turbulence kinetic energy in separated turbulent flows over curved surfaces are yet to be conducted.

We have recently developed a new projection method, called FastRK3, to solve the incompressible Navier-Stokes (NS) equations in orthogonal curvilinear coordinates [6]. FastRK3 is an explicit, three-stage, third-order Runge-Kutta based projection-method which requires solving the Poisson equation for pressure only once per time step versus three times by standard RK3 methods. In the current paper, we present the DNS results obtained by using FastRK3, of an incompressible turbulent boundary layer separating over a curved ramp which is similar to the circular arc experimentally studied by Song and Eaton [7].

2 Mathematical description

2.1 Governing equations

The NS equations for an incompressible flow in orthogonal curvilinear coordinates are [6]

$$\nabla_i \hat{U}^i = 0, \quad (1)$$

$$\frac{\partial \hat{U}^i}{\partial t} + \nabla_j \hat{U}^i \hat{U}^j = -\frac{1}{\rho} g^{ij} \nabla_j p + \nu g^{jk} \nabla_{jk}^2 \hat{U}^i, \quad (2)$$

where $\boldsymbol{\xi} = \xi^i \mathbf{g}_i = (\xi, \eta, \zeta)$, where \mathbf{g}_i are the covariant basis vectors, $\mathbf{U}(\boldsymbol{\xi}, t) = \hat{U}^i \mathbf{g}_i$ is the fluid velocity expressed in contravariant components (see Fig. 2 of [6]), $p(\boldsymbol{\xi}, t)$ is the pressure. ν is the fluid kinematic viscosity, ρ is the fluid density, g^{ij} is the inverse of the metric tensor g_{ij} ($g_{ij} g^{jk} = \delta_j^k$, the Kronecker symbol), and the covariant derivative operator ∇_k is defined as

$$\nabla_k \hat{U}^j = \frac{\partial \hat{U}^j}{\partial \xi^k} + \Gamma_{ik}^j \hat{U}^i, \quad (3)$$

where Γ_{jk}^i are the Christoffel symbols of second kind and g_{ij} is the metric tensor, which relates distance to the infinitesimal coordinate increments [8]. In orthogonal coordinates, the off-diagonal terms of the metric tensor are identically zero: $g_{ij} = 0, \forall i \neq j$.

2.2 Pressure-correction method: FastRK3

The incompressible NS equations can be written in their spatially discretized form [6] as

$$\begin{aligned} DU + b(t) &= 0, \\ \frac{dU}{dt} &= F(U) - \frac{Gp}{\rho}, \end{aligned} \quad (4)$$

where, $U(t)$ and $p(t)$ are the arrays of the discretized three-dimensional contravariant components of velocity and pressure, respectively, D is the discretized divergence operator, $b(t)$ is a smooth function that accounts for unsteady boundary conditions, F is the combined array of discretized terms of convection $C = C(U)$ and diffusion VU of momentum, where $C(U)$ is the discrete form of $\nabla \cdot \mathbf{u}\mathbf{u}$, and VU is the discrete form of $\text{Re}^{-1} \nabla^2 \mathbf{u}$,

$$F(U) = C(U) + VU, \quad (5)$$

and G is the discretized gradient operator. It should be noted that C and by extension F are non-linear functions of U , i.e., $F(U)$ and $C(U)$, whereas V is a linear operator ($\text{Re}^{-1} \nabla^2$) applied to U , i.e., VU .

For an explicit RK3 scheme, the Butcher tableau [9] is given by

$$\begin{array}{c|ccc} 0 & 0 & & \\ c_2 & a_{21} & 0 & \\ c_3 & a_{31} & a_{32} & 0 \\ \hline & b_1 & b_2 & b_3 \end{array} \quad (6)$$

Note that $i = 1, 2, 3$ corresponds to the three stages of the RK3 scheme where the numerical solution is advanced in time from t_n to t_{n+1} with the time of each i -stage as $t_i = t_n + \tilde{c}_i \Delta t$, where $\Delta t = t_{n+1} - t_n$. We define a shifted coefficient matrix $\tilde{\mathbf{a}}$ and a shifted vector $\tilde{\mathbf{c}}$ similarly to SK [10]:

$$\tilde{\mathbf{a}} = \begin{bmatrix} a_{21} & 0 & 0 \\ a_{31} & a_{32} & 0 \\ b_1 & b_2 & b_3 \end{bmatrix}; \quad \tilde{\mathbf{c}} = \begin{bmatrix} c_2 \\ c_3 \\ 1 \end{bmatrix}. \quad (7)$$

For the pressure-correction method [11], the solution algorithm begins with the computation of the approximate velocity field U^* , which is not divergence free. U_n and U_{n+1} denote the divergence-free velocity fields

at t_n and t_{n+1} , respectively. At each stage i of the RK3 scheme, U_i^* denotes the approximate velocity field, U_i the divergence-free velocity field, and ϕ_i the pressure-like scalar field.

U_n and U_{n+1} denote the velocity fields at time t_n and t_{n+1} , respectively. At each stage i of FastRK3 by [6], U_i^* denotes the approximate velocity field, U_i the divergence-free velocity field, and p_i the pressure field:

$$U_3 \equiv U_{n+1}; \quad U_3^* \equiv U_{n+1}^*; \quad \phi_3 \equiv \phi_{n+\frac{1}{2}}; \quad U_0 \equiv U_n; \quad U_0^* \equiv U_n; \quad c_0 \equiv 0. \quad (8)$$

The discretized governing equations (4) are integrated in time using the FastRK3 scheme:

$$U_i^* = U_n + \Delta t \sum_{j=1}^i \tilde{a}_{ij} F \left(U_{j-1}^* - \tilde{c}_{j-1} \Delta t \frac{G\phi_{j-1}}{\rho} \right) \quad \text{for } i = 1, 2, 3, \quad (9)$$

where i denotes the stage of RK3. For FastRK3 [6], the Poisson equation for pressure is solved only once per time step, at the final stage $i = 3$. Therefore, $G\phi_1$ and $G\phi_2$ are approximated by performing a linear extrapolation of the gradient of ϕ in time, using the known values of $\phi_{n-\frac{1}{2}}$ and $\phi_{n-\frac{3}{2}}$ using the midpoint (MP) formulation [12], which achieves second-order temporal accuracy for velocity and pressure for ‘stiff’ wall-bounded flows as proved in [12], as

$$\phi_1 = \left(\frac{3 + \tilde{c}_1}{2} \right) \phi_{n-\frac{1}{2}} - \left(\frac{1 + \tilde{c}_1}{2} \right) \phi_{n-\frac{3}{2}}, \quad (10)$$

$$\phi_2 = \left(\frac{3 + \tilde{c}_2}{2} \right) \phi_{n-\frac{1}{2}} - \left(\frac{1 + \tilde{c}_2}{2} \right) \phi_{n-\frac{3}{2}}. \quad (11)$$

Then, the velocity field at t_{n+1} is obtained by applying the pressure-correction at the final stage, $i = 3$, as

$$U_{n+1} = U_{n+1}^* - \Delta t G \phi_{n+\frac{1}{2}} / \rho, \quad (12)$$

where $\phi_{n+\frac{1}{2}}$ is obtained by solving the Poisson equation using the FastPoc solver,

$$DG\phi_{n+\frac{1}{2}} = \rho (DU_{n+1}^* + b_{n+1}) / \Delta t, \quad (13)$$

which is obtained by taking the divergence of Eq. (12) while imposing the divergence-free condition for U_{n+1} . The pressure field p_{n+1} can then be computed using the update equation of [10] (see Eq. (67) of [10]), as

$$p_{n+1} = -\frac{3}{2} \left[\left[3 + \frac{(\tilde{c}_1 + \tilde{c}_2)}{2} \right] \phi_{n-\frac{1}{2}} - \left[1 + \frac{(\tilde{c}_1 + \tilde{c}_2)}{2} \right] \phi_{n-\frac{3}{2}} \right] + 4\phi_{n+\frac{1}{2}}. \quad (14)$$

Sanderse and Koren [10] note that the pressure field p_{n+1} is at best second-order accurate. The coefficients for the three-stage, third-order explicit Runge-Kutta scheme are [10]:

$$\tilde{\mathbf{a}} = \begin{bmatrix} \frac{1}{3} & 0 & 0 \\ -1 & 2 & 0 \\ 0 & \frac{3}{4} & \frac{1}{4} \end{bmatrix}; \quad \tilde{\mathbf{c}} = \begin{bmatrix} \frac{1}{3} \\ 1 \\ 1 \end{bmatrix}. \quad (15)$$

In summary, our new pressure-correction algorithm advances the numerical solution of the velocity field in time by integrating Eq. (4) with the following steps using Eqs. (9)-(13):

1. At the first stage ($i = 1$) of FastRK3, compute $F(U_n)$, and then compute U_1^* using Eq. (9),
2. For the second stage ($i = 2$) of FastRK3, compute $G\phi_1$ using Eq. (10) and $F(U_1^* - \tilde{c}_1 \Delta t G\phi_1)$, and then compute U_2^* using Eq. (9),
3. At the third stage ($i = 3$) of FastRK3, compute $G\phi_2$ using Eq. (11) and $F(U_2^* - \tilde{c}_2 \Delta t G\phi_2)$, and then compute $U_{n+1}^* = U_3^*$ using Eq. (9),
4. Compute $\phi_{n+\frac{1}{2}}$ by solving the Poisson equation (13) using U_{n+1}^* and a Poisson solver, e.g., the FastPoc method described in [6],

5. Compute U_{n+1} using Eq. (12), and, if the pressure is desired for post-processing, compute p_{n+1} using Eq. (14).

2.3 Fast Poisson solver for orthogonal coordinates: FastPoc

One of the key aspects of our flow solver, FastRK3, is that the choice of the orthogonal formulation of NS equations has enabled us to develop and use, for the first time for such flows, an FFT-based Poisson solver for pressure, called FastPoc [6]. The Poisson equation for pressure in orthogonal curvilinear coordinates is a variable-coefficient Poisson equation which is typically solved using multigrid methods. However, the multigrid methods are computationally more expensive than direct FFT-based methods (e.g., [13]). The choice of orthogonal curvilinear coordinates results in the absence of cross derivatives in the Poisson equation for pressure. Further, for the flows over curved surfaces here considered: surfaces of linear translation the computational domain does not present variations in the azimuthal ζ direction. Therefore, we perform real-to-complex FFT along the ζ -direction to reduce the three-dimensional system of linear equations to two-dimensional systems of linear equations. We have also developed a new 3D transpose algorithm, similarly to the all-to-all zero-copy method of Hoefler & Gottlieb [14] to perform the required 3D transpose of data among processors. The resulting two-dimensional systems of linear equations are then solved using the HSL ME57 direct, serial, linear-solver [15] which uses the LDL^T decomposition [16] implemented using a multifrontal approach. We use the fill-in reducing nested-dissection ordering [16, 17] produced by METIS [18] for the sparse coefficient matrices to reduce the storage and computational costs of matrix factorization. We have shown that FastPoc is thirty to sixty times faster than *hypre* SGS multigrid [19] for tolerance set at 10^{-6} and 10^{-12} , respectively, and the entire NS solver, FastRK3, is four to seven times faster when using FastPoc rather than multigrid accordingly to these set tolerance values [6].

In FastRK3, the NS equations in the orthogonal formulation are discretized in space on a staggered grid using the second-order central-difference scheme. FastRK3 has been verified, validated and produces nearly identical results to standard RK3 [6]. The absence of cross derivatives in the orthogonal formulation of NS equations results in a significant reduction in the number of terms to be computed and has also enabled us to develop and use in FastRK3 an FFT-based Poisson solver for pressure, called FastPoc. These properties make FastRK3 a faster method than those relying on three Poisson solvers per time step, e.g., standard RK3 methods, and/or using multigrid to solve the Poisson equation for pressure.

2.4 Flow domain

We have applied FastRK3, to simulate the spatially developing turbulent boundary layer over the curved ramp experimentally studied by [7]. Figure 1 shows a schematic of the flow domain used in the experiments. The ramp is a circular arc with a radius $R = 127\text{mm}$. The ramp height h and length L are 21mm and 70mm, respectively. [7] define a reference station (x_r) two ramp-lengths upstream of the ramp. We place the inflow plane of the DNS at the reference station with the Reynolds number based on inflow boundary layer thickness $Re_{\delta_0} = 1/\nu = 9000$, where ν is the dimensionless kinematic viscosity, such that the inflow $Re_{\theta_0} = 1100$. The ramp profile used in the experiments has a discontinuity of its first-derivative at the location where the circular arc ends intersecting the horizontal wall (Fig. 1). We eliminate this discontinuity by using spline interpolation in a small region ($0.9 \leq x/L \leq 1$) in order to generate a smooth orthogonal mesh over the ramp (Fig. 2). Figure 2 shows the computational domain used in our simulations. The length scales non-dimensionalized by the boundary layer thickness at the inflow plane, $\delta_0 = 25.6\text{mm}$, are

$$L_r = 5.47\delta_0, \quad L = 2.73\delta_0, \quad L_s = 13.67\delta_0, \quad R = 4.96\delta_0, \quad h = 0.82\delta_0. \quad (16)$$

The dimensions of the computational domain, L_ξ , L_η and L_ζ , normalized by δ_0 , and the number of grid points, N_x , N_y and N_z in the streamwise, wall-normal and spanwise directions, respectively, are listed in Table 1. As shown in Fig. 2, we define the coordinate system such that the streamwise coordinate (ξ or x) of the leading edge of the ramp is set to zero and the wall-normal coordinate (η or y) are always zero at the wall. The non-dimensional quantities in wall-units carry the superscript ‘+’, i.e., $\langle \hat{U} \rangle^+ = \langle \hat{U} \rangle / u_\tau$ and $\eta^+ = \eta u_\tau / \nu$, where $\langle \dots \rangle$ represents the spatial averaging in the spanwise ζ -direction in addition to time averaging of the enclosed quantity, $u_\tau = \sqrt{\tau_w / \rho}$ is the friction velocity, τ_w is the wall shear stress, and ρ

is the fluid density. The zero subscript refers to the conditions at the inflow plane where $Re_{\theta_0} = 1100$ at $x/L = -2$ from the ramp as in the experiments.

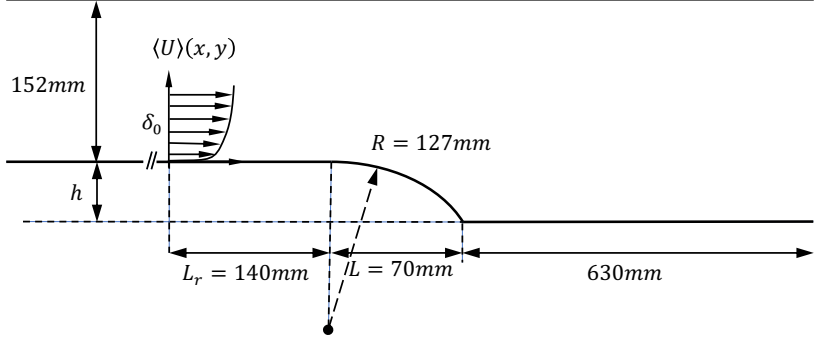


Figure 1: Flow schematic of the experiment of [7].

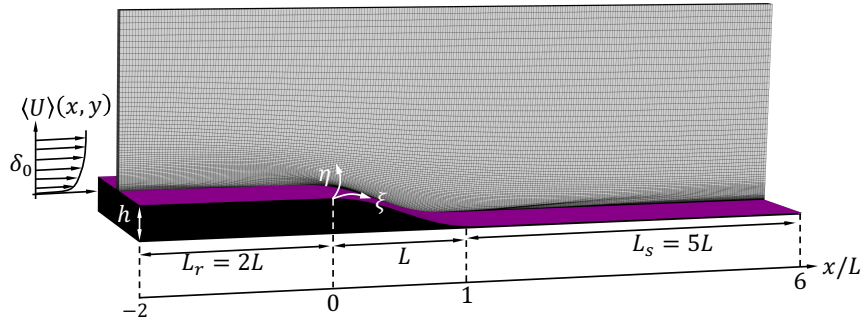


Figure 2: Computational domain used in the present DNS.

The grid spacing is $\Delta\xi^+ = 8$, $\Delta\eta_{\min}^+ = 0.7$ and $\Delta\zeta^+ = 12$, where the grid in the wall-normal direction is stretched gradually to have a fine grid close to the wall. We use the grid-stretching function given by [20] and the grid stretching parameter is $\gamma = 0.66$. The turbulent inflow conditions were generated with the method of [20]. The timestep size is $\Delta t = 0.03\nu/u_\tau^2$ and we advance the solution up to $T = 450 \approx 8100\nu/u_\tau^2$ and compute the statistics every ten timesteps during the time interval $150 \leq t \leq 450$ which corresponds to 25 flow-throughs at a non-dimensional velocity of $0.9U_\infty$.

L_x	L_y	L_z	N_x	N_y	N_z
$20\delta_0$	$4\delta_0$	$10\delta_0$	1024	128	512

Table 1: The dimensions of the computational domain, L_x , L_y and L_z , and the number of grid points, N_x , N_y and N_z in the streamwise, wall-normal and spanwise directions, respectively.

3 Results

3.1 Mean velocity profiles

Figure 3 shows the contours of the mean Cartesian streamwise ($\langle U \rangle / U_\infty$) and wall-normal ($\langle V \rangle / U_\infty$) components of velocity. Figure 3b shows the separation bubble along with the streamlines and the isoline where $\langle U \rangle = 0$. The mean pressure contour $\langle p \rangle$ is shown in Fig. 4a. Figure 4 shows the profiles of mean Cartesian streamwise ($\langle U \rangle / U_\infty$) and wall-normal ($\langle V \rangle / U_\infty$) components of velocity. We identify eight streamwise stations (A-H) where each station is represented by a color whose lightness value increases sequentially downstream of the inflow plane as shown in Fig. 4. The velocity profiles at B are already affected by the presence of the ramp and show deviations from the flat-plate behavior of station A. Typically, $\langle V \rangle / U_\infty \ll 1$ for flat-plate TBL, however, we see that $|\langle V \rangle| / U_\infty \approx \mathcal{O}(1)$ at stations B-G. The flow decelerates due to the adverse pressure gradient and eventually separates at C. We observe reversed flow at stations D and E and the flow reattaches at F. The flow, then, starts to returning to its characteristics (e.g., mean velocity profiles and Reynolds stresses) of a ZPG-SDTBL, as seen in stations G and H. Figure 5 also shows the spatial development of the skin friction coefficient c_f .

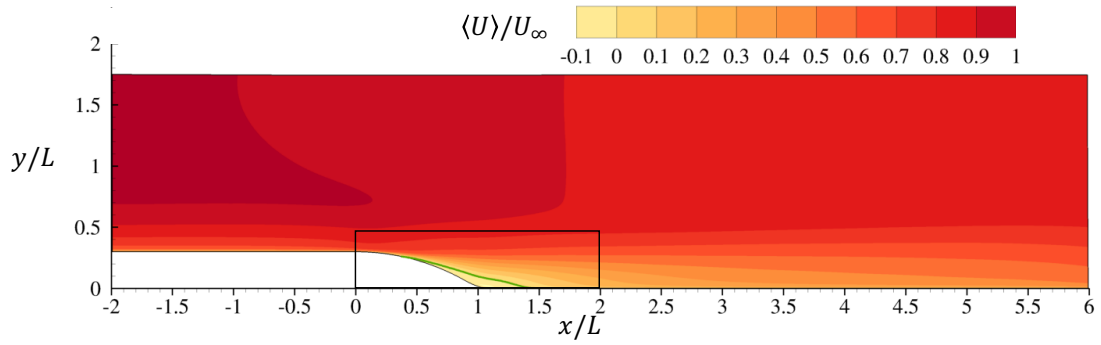
3.2 Turbulence kinetic energy and Reynolds stresses

Figures 6a and 6b show the profiles and color contours, respectively, of the turbulence kinetic energy (TKE), k_0^+ , normalized by the viscous scales at $x_0 = -2L$. In the region upstream of the ramp ($x < 0$), the peak values of TKE are obtained close to the wall. However, in the separated region and in the recovery region ($x > 0.4L$), the peak TKE shifts away from the wall due to the enhanced turbulence present in the separated region and the recovery region of the flow. The components of Reynolds stresses shown in Fig. 7 also exhibit a similar behavior. Stations A and B show the profiles of Reynolds stresses similar to those of a ZPG flat-plate boundary layer. We see a departure from this starting from station C down to station F, and the peaks of the profiles shift away from the wall due to the separation bubble. Downstream of the reattachment location, we see the Reynolds stress profiles returning to their characteristic ZPG flat-plate boundary layer behavior. In Sec. 3.3, we study the budget of k_0^+ at the A ($x = -2$) and E ($x = L$) stations.

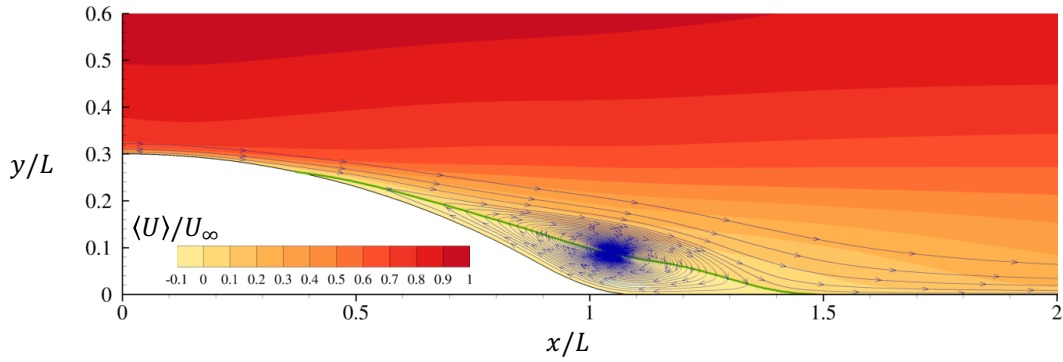
3.3 Turbulence kinetic energy budget

Figures 8a and 8b show the budget of TKE, k_0^+ , at A ($x = -2L$) and E ($x = L$), respectively. The budget of k_0^+ at A ($x = -2L$) exhibits similar characteristics as that of a flat-plate turbulent boundary layer discussed by Pope [21]. Dissipation reaches its peak value at the wall, while production peaks in the buffer layer at $y_0^+ \approx 11$. Production exceeds dissipation around the y -location of peak TKE and the excess energy is carried away by the transport terms. The viscous diffusion term transports kinetic energy all the way to the wall.

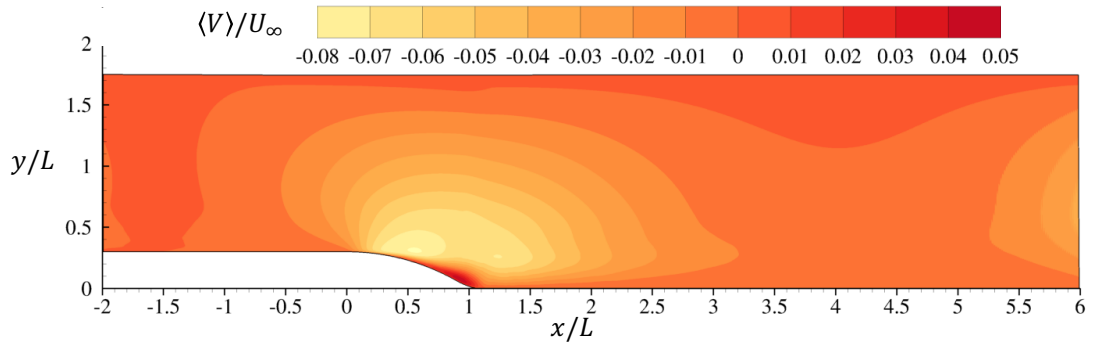
The budget of k_0^+ at E ($x = L$) differs greatly from the typical behavior of a flat-plate turbulent boundary layer. The peak production is obtained at $y_0^+ \approx 240$ which is indicative of the fact that the vigorous turbulent activity in the flow has shifted away from the wall due to the separation bubble. Around this peak, production exceeds dissipation and the excess energy is carried away by the transport terms, including the pressure. The peak dissipation is still obtained at the wall and the viscous diffusion term transports kinetic energy all the way to the wall. Finally, we will investigate the Reynolds stress balances to better understand the dynamics of turbulence in this separated flow over the curved wall.



(a) Color contours of the mean Cartesian x -component of velocity $\langle U \rangle / U_\infty$ and the isoline (green) where $\langle U \rangle = 0$.

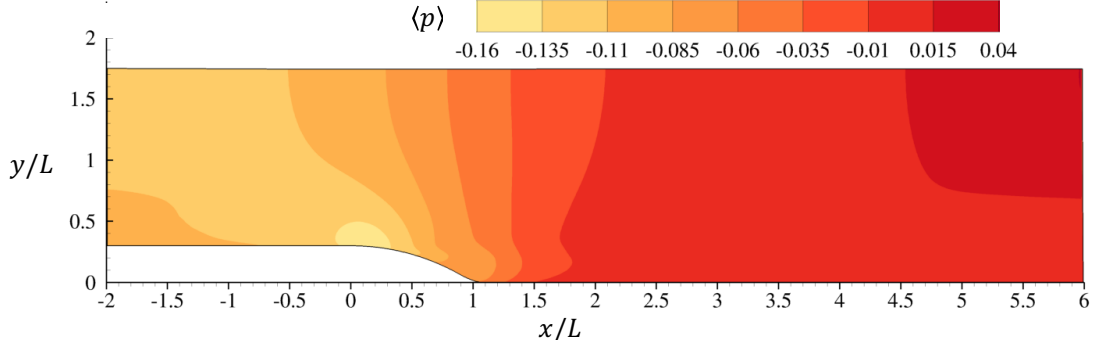


(b) The subdomain of Fig. 3a showing the separation bubble along with the streamlines and isoline (green) where $\langle U \rangle = 0$.

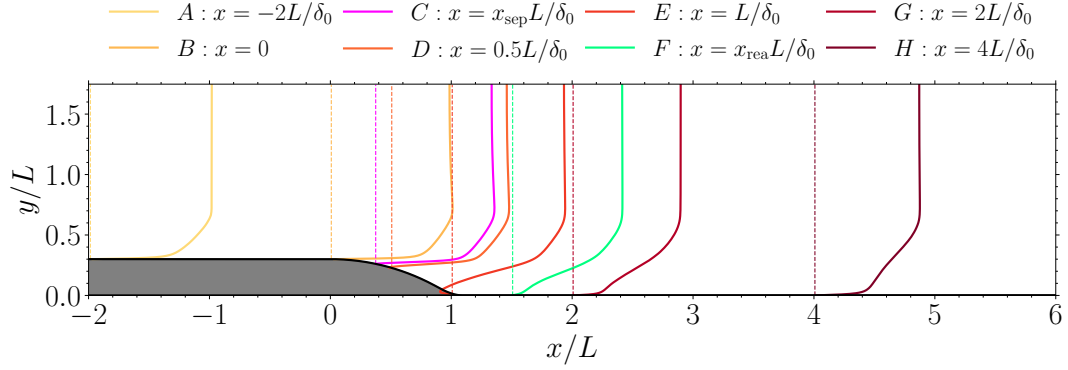


(c) Color contours of the mean Cartesian y -component of velocity $\langle V \rangle / U_\infty$.

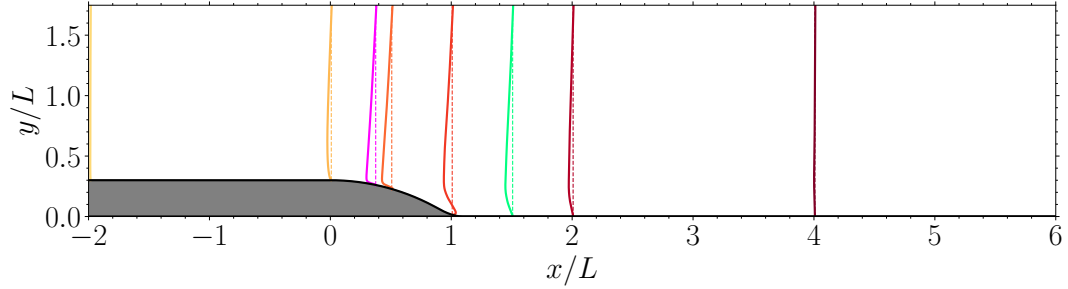
Figure 3: Color contours of x - and y -components of mean Cartesian velocity.



(a) Color contours of the mean pressure $\langle p \rangle$.



(b) Mean Cartesian x -component of velocity $\langle U \rangle/U_\infty$ (solid lines) at streamwise stations: A-H (dotted lines).



(c) Mean Cartesian y -component of velocity $\langle V \rangle/U_\infty$ (solid lines) at streamwise stations: A-H (dotted lines).

Figure 4: (a) Color contours of mean pressure, and (b) and (c) profiles of the mean Cartesian x - and y -components of velocity, respectively, at streamwise stations A-H.

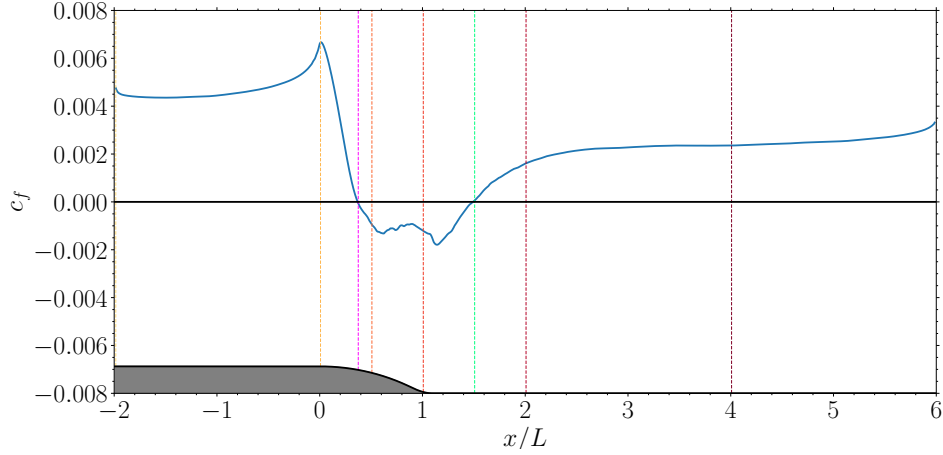
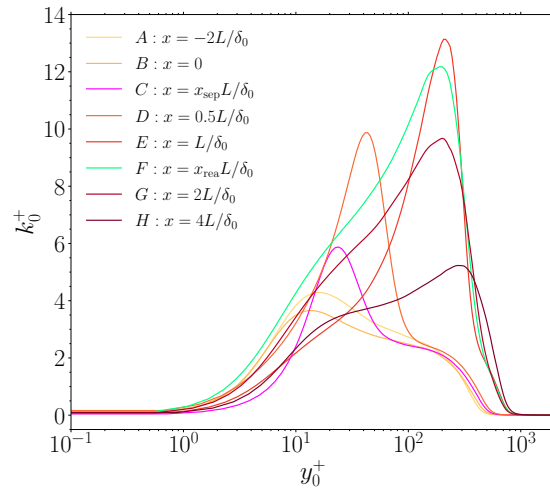
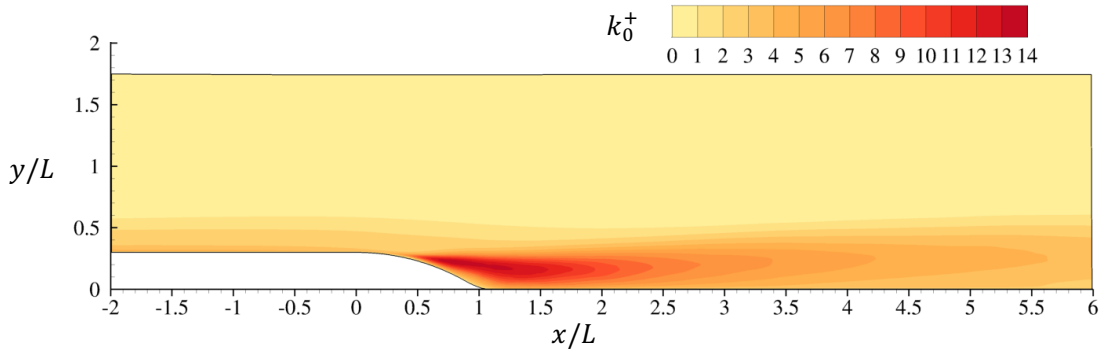


Figure 5: Spatial development of c_f along the streamwise direction.



(a) Profiles of turbulence kinetic energy, k_0^+ at x -stations A-H. Wall units are normalized by viscous scales at $x_0 = -2L$.



(b) Color contours of the turbulence kinetic energy k_0^+ . Wall units are normalized by viscous scales at $x_0 = -2L$.

Figure 6: (a) Profiles and (b) color contours of the turbulence kinetic energy k_0^+ .

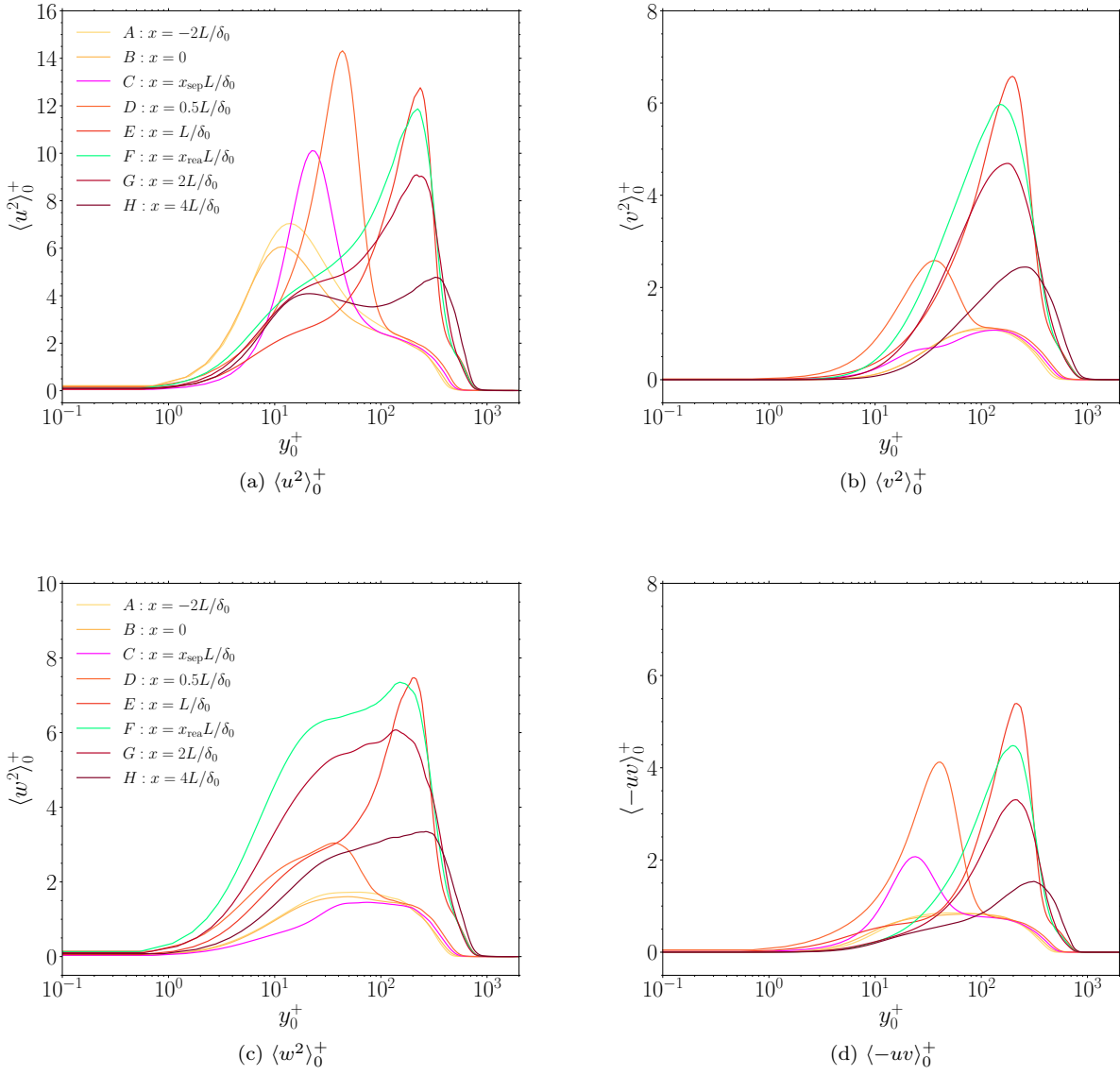


Figure 7: Components of Reynolds stresses at x -stations A-H. Wall units are normalized by viscous scales at $x_0 = -2L$.

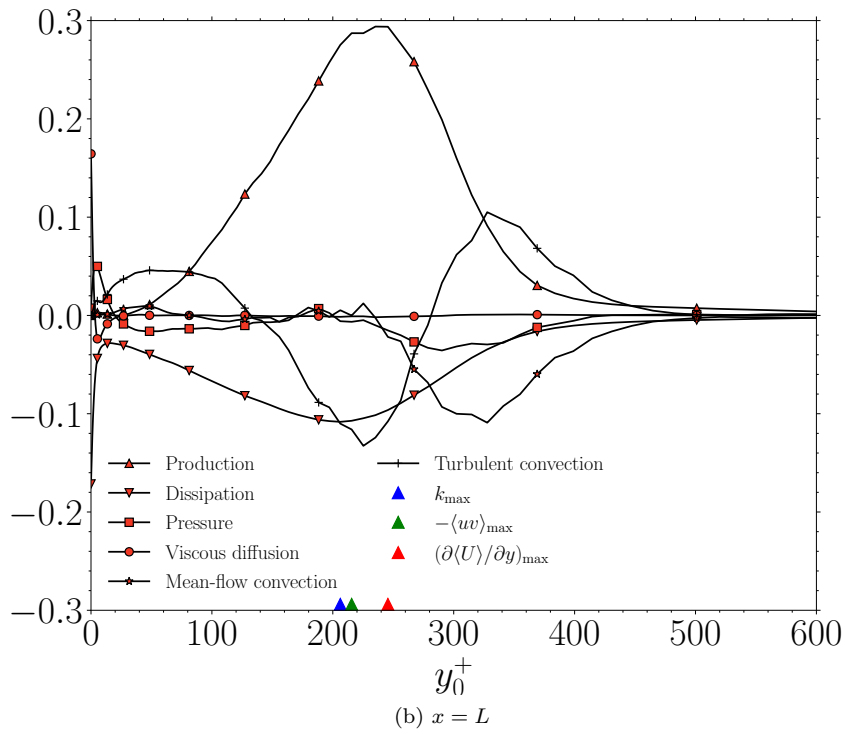
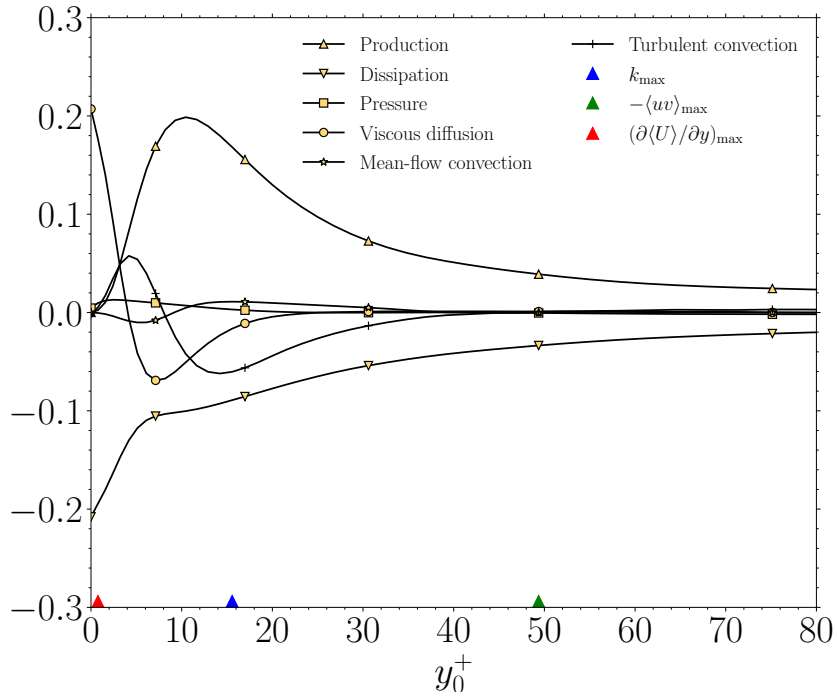


Figure 8: Budget of turbulence kinetic energy normalized by viscous scales at $x_0 = -2L$ and $x = L$. Positions of maximum values of k , $-\langle uv \rangle$ and $\partial \langle U \rangle / \partial y$ are denoted by triangles on horizontal axis.

References

- [1] R. L. Simpson, Turbulent boundary-layer separation, *Annu. Rev. Fluid Mech.* 21 (1) (1989) 205–232.
- [2] J. Fröhlich, C. P. Mellen, W. Rodi, L. Temmerman, M. A. Leschziner, Highly resolved large-eddy simulation of separated flow in a channel with streamwise periodic constrictions, *J. Fluid Mech.* 526 (2005) 19–66.
- [3] O. Williams, M. Samuelli, E. S. Sarwas, M. Robbins, A. Ferrante, Experimental study of a CFD validation test case for turbulent separated flows, in: *AIAA Scitech 2020 Forum*, 2020, p. 0092.
- [4] J.-P. Mollicone, F. Battista, P. Gualtieri, C. Casciola, Effect of geometry and Reynolds number on the turbulent separated flow behind a bulge in a channel, *J. Fluid Mech.* 823 (2017) 100–133.
- [5] R. Balin, K. E. Jansen, Direct numerical simulation of a turbulent boundary layer over a bump with strong pressure gradients, *J. Fluid Mech.* 918.
- [6] A. B. Aithal, A. Ferrante, A fast pressure-correction method for incompressible flows over curved walls, *J. Comput. Phys.* 421 (2020) 109693. doi:<https://doi.org/10.1016/j.jcp.2020.109693>.
- [7] S. Song, J. K. Eaton, Reynolds number effects on a turbulent boundary layer with separation, reattachment, and recovery, *Experiments in fluids* 36 (2) (2004) 246–258.
- [8] R. Aris, *Vectors, Tensors and the Basic Equations of Fluid Dynamics*, Prentice-Hall, 1962.
- [9] J. C. Butcher, *Numerical methods for ordinary differential equations*, John Wiley & Sons, 2016.
- [10] B. Sanderse, B. Koren, Accuracy analysis of explicit Runge-Kutta methods applied to the incompressible Navier-Stokes equations, *J. Comput. Phys.* 231 (8) (2012) 3041–3063.
- [11] F. H. Harlow, J. E. Welch, Numerical calculation of time-dependent viscous incompressible flow of fluid with free surface, *Phys. Fluids* 8 (1965) 2182–2189.
- [12] A. B. Aithal, M. Tipirneni, A. Ferrante, Temporal accuracy of FastRK3, *J. Comput. Phys.*, Under review.
- [13] M. S. Dodd, A. Ferrante, A fast pressure-correction method for incompressible two-fluid flows, *J. Comput. Phys.* 273 (2014) 416–434.
- [14] T. Hoefler, S. Gottlieb, Parallel zero-copy algorithms for fast Fourier transform and conjugate gradient using MPI datatypes, in: *European MPI Users’ Group Meeting*, Springer, 2010, pp. 132–141.
- [15] HSL, HSL: A collection of Fortran codes for large scale scientific computation, <http://www.hsl.rl.ac.uk> (2013).
- [16] A. George, Nested dissection of a regular finite element mesh, *SIAM Journal on Numerical Analysis* 10 (2) (1973) 345–363.
- [17] R. J. LeVeque, *Finite difference methods for ordinary and partial differential equations: steady-state and time-dependent problems*, Vol. 98, SIAM, 2007.
- [18] G. Karypis, V. Kumar, MeTis: Unstructured graph partitioning and sparse matrix ordering system, version 4.0, <http://www.cs.umn.edu/metis> (2009).
- [19] R. D. Falgout, J. E. Jones, U. M. Yang, The design and implementation of hypre, a library of parallel high performance preconditioners, in: *Numerical solution of partial differential equations on parallel computers*, Springer, 2006, pp. 267–294.
- [20] A. Ferrante, S. E. Elghobashi, A robust method for generating inflow conditions for direct simulations of spatially-developing turbulent boundary layers, *J. Comput. Phys.* 198 (1) (2004) 372–387.
- [21] S. B. Pope, *Turbulent Flows*, Cambridge Univ. Press, 2000.